PCCP

ROYAL SOCIETY OF CHEMISTRY

PAPER

View Article Online
View Journal | View Issue

Check for updates

Cite this: *Phys. Chem. Chem. Phys.*, 2021, **23**, 2780

Redox-couple investigations in Si-doped Li-rich cathode materials†

Leah Nation, *[a] Yan Wu,[b] Xiaoming Liu,[c] Miaofang Chi, [c] Yuqin Wu,[d] Yue Qi [d] and Brian W. Sheldon *[a]

Received 4th November 2020,
Accepted 8th January 2021

DOI: 10.1039/d0cp05737a

rsc.li/pccp

In this investigation, the improved electrochemical behavior in Si-doped Li-rich cathodes is studied with scanning transmission electron microscopy (STEM) and electron energy loss spectroscopy (EELS). Z-contrast images show a layered structure that develops a thin, spinel-like surface layer after the first charge cycle. Si-doping increases discharge capacity by ∼25% and appears to retard the surface phase transformation. Based on electron energy loss spectra, the surface layer in the doped material has an altered oxygen electronic environment, which supports the STEM findings. Furthermore, Si-doping changes the redox behavior during the activation cycle. Density functional theory calculations indicate that Si-doping can increase oxygen vacancy formation, and change the sequence of the redox couples by introducing more oxygen vacancies before or during the typical high voltage activation process. The results of this work indicate that the type of doping employed here is an effective strategy for controlling the complex charge compensation mechanisms in lithium-rich cathodes.

I. Introduction

Lithium-rich oxides hold great promise as next-generation lithium-ion battery cathode materials as they exhibit high energy density due to oxygen vacancy formation and reversible anionic redox in addition to cationic redox.[1–4] Oxygen redox occurs when the energy of the transition metal band is below the oxygen band. In lithium-rich cathodes with Li–O–Li configurations, the oxygen band is shifted such that its electrons are more easily extracted.[5] Excess oxygen redox and oxygen loss facilitate cation rearrangement and surface phase transformation leading to voltage and capacity fade.[6–9] The complex structural changes and corresponding degradation that occur during electrochemical cycling are not well understood at this time. Coatings and doping schemes are widely employed to improve the performance of lithium-rich materials[10–15] by stabilizing the layered structure, changing the microstructure, or improving conductivity. The shift in activation potentials of different lithium-rich compositions suggests there is an energy barrier to anionic redox, and that doping can be used to modulate oxygen redox.[16] Si-doping has been demonstrated to increase the capacity of $Li_{1.2}Mn_xNi_yCo_{0.8-x-y}O_2$ (HE-NMC) and stabilize the structure during cycling.[17,18]

The experiments reported here focus on a systematic investigation of Si-doping. Scanning transmission electron microscopy (STEM) is used to characterize the surface and bulk structure of control and Si-doped HE-NMC in the pristine and charged states. Electron energy loss spectroscopy (EELS) is used to probe the electronic states of Ni, Mn, Co, and O in the control and Si-doped HE-NMC materials. These data provide detailed information about the impact of Si-doping on changes that occur during the first charge cycle and differences between the surface and the bulk of cycled samples. Density functional theory (DFT) predictions support the experimental findings and suggest that Si-doping promotes the formation of oxygen vacancies, which in turn alters redox behavior during the activation cycle. The overall findings demonstrate that this type of doping can be used to alter degradation processes and improve performance, in ways that differ considerably from other strategies that have been employed with HE-NMC cathodes.

II. Experiments and modeling

$Li_{1.2}Mn_{0.54}Ni_{0.13}Co_{0.13}O_2$ and $Li_{1.2}Mn_{0.49}Si_{0.05}Ni_{0.13}Co_{0.13}O_2$ powders were synthesized using the co-precipitation method described previously.[17] A slurry of 80 : 10 : 10 active material: PVDF binder: conductive carbon was coated at a 10 mil wet

---

[a] School of Engineering, Brown University, Providence, RI, 02912, USA. E-mail: brian_sheldon@brown.edu

[b] General Motors Technical Center, Warren, MI, 48092, USA

[c] Center for Nanophase Materials Sciences, Oak Ridge National Laboratory, Oak Ridge, TN, 37831, USA

[d] Department of Chemical Engineering and Materials Science, Michigan State University, East Lansing, Michigan, 48824, USA

† Electronic supplementary information (ESI) available. See DOI: 10.1039/d0cp05737a

thickness onto aluminum foil and dried at 80 °C. Coin cells were assembled in an argon filled glovebox with lithium metal counter electrode, Celgard 2325 separator and 1 M $LiPF_6$ in 1/1 EC/DEC electrolyte. First cycle voltage measurements were conducted at C/100 and rate capability cycling conditions ranged from C/20–2C, where the 1C current corresponds to approximately 2 mA and 1.6 mg cm^{-2} loading.

For transmission electron microscopy (TEM) characterization, cells were charged at a C/10 rate to 4.4 V (cutoff voltage before activation) and 4.6 V (cutoff voltage after activation) and disassembled after the first charge cycle. Charged electrodes were harvested in the glovebox, rinsed in DMC, and dried. The dried electrode was then scraped off the current collector for STEM and EELS post-mortem characterization. Sample powders were loaded onto a lacy carbon grid for STEM/EELS analysis which were performed with an aberration corrected FEI Titan microscope at 300 kV equipped with a Gatan Image Filter Quantum-865. HAADF-STEM images were recorded with a probe convergence angle of 30 mrad and a large inner collection angle of 65 mrad. Lithium layers were distinguished from the transition metal layers by Z contrast imaging in which heavier atoms appear brighter. Image J was used on the STEM images to perform a Fourier transform as well as measure lengths. STEM images and EELS were collected separately from nearby regions to ensure minor damage from the electron beam. The electron beam can artificially change the position of the transition metal edges, so only relative energy shifts are reported. Ten pixels per spectrum were summed to increase the signal to noise ratio. These pixels include contributions from both the surface and bulk regions, which makes it difficult to interpret spatial element maps from a given particle (because the relative surface and bulk contributions vary with particle size and at different positions across a given particle). For comparisons within a particle from the surface to bulk, single pixels were analyzed. The background was removed using Digital Micrograph software through a power-law fitting in the pre-edge region of each spectrum using a consistent background window. The stoichiometry was estimated using Digital Micrograph's quantification feature. Both the white line ratio and edge onset methods were used to measure the chemical shift of the transition metals. The white line ratio can be affected by the sample thickness whereas the edge onset method is independent of thickness.[19]

The EELS in strongly-correlated systems and materials with large core-hole effects, such as the cathode materials studied here, cannot be accurately described with DFT methods. However, some rationalization based on electronic structures can still be obtained from DFT calculations. Therefore, to further examine the role of Si-doping, the electronic structure of Si-doped Li_2MnO_3 was simulated. Li_2MnO_3 serves as a model material for studying the Li-rich NMCs.[20] In Li_2MnO_3, the oxygen atoms are in the Li–O–Li configuration which is associated with interesting redox behavior in the lithium-excess materials that are studied here. The Si is substituted on Mn sites, and to simplify the analysis the Ni and Co are not included. This structure provides relevant insight into the doping effects, since Si substitutes for Mn in the Li-rich cathodes employed in the experiments. A 2 × 1 × 2 Li_2MnO_3 supercell (96 atoms) was constructed, with Si substitution on one of the 16 Mn sites (6.25% dopant level). The DFT computations presented here were performed using Vienna Ab initio Simulation Package (VASP).

The generalized gradient approximation (GGA) with a 4.84 eV Hubbard U correction for Mn was adopted for parametrization of the exchange–correlation functional. To optimize the structure, a plane-wave cutoff energy of 550 eV, larger than 1.3 times the suggested maximum cutoff in the VASP pseudopotentials, were used. A 3 × 3 × 3 Monkhorst–Pack grid were applied, having over $(1000)/n$ grid points, where n denotes the number of atoms in the unit cell. The optimization was done when the energy convergence of 0.2 meV per atom was reached. Density of states were analyzed to illustrate the electronic structure change.

III. Results and discussion

3.1 Characterization of materials

The atomic ratio of the pristine powders was quantified based on EELS spectra. The results are shown in Table 1 and compared with the expected ratios based on the formulation stoichiometry. The concentration differences in pristine materials agree with stoichiometric formulations. As expected by the formulation, the quantification method determined that the silicon substitution of manganese in the doped material reduces the manganese by about 10%.

The electrochemical performance of the HE-NMC materials was evaluated using galvanostatic cycling at various rates. Fig. 1a shows the first charge voltage profiles. The doped and undoped materials have similar capacity during the activation cycle. However, the breakdown between the sloping region to 4.4 V and the plateau around 4.5 V is different, with a shorter sloping region and a longer plateau in the control material. After the activation cycle at C/20 the rate capability were obtained during subsequent testing with 2 cycles each at C/10, C/5, 2C/3, 1C, and 2C discharge. The values for the two cycles at each rate were very similar, and the average values are shown in Fig. 1b. These results show that the discharge capacity of the doped material is ∼25% higher at all rates tested.

Fig. 2 shows representative high resolution HAADF-STEM images of the control and Si-doped HE-NMC samples in the pristine and charged state. The material is highly crystalline with a well ordered layered structure. The image contrast represents changes in the atomic weight, with brighter areas

Table 1 The atomic ratio of pristine powders found using digital micrograph and expected based on formulation

	Pristine control HE-NMC		Pristine $Si_{0.05}$ HE-NMC	
Element	Determined	Expected	Determined	Expected
O	1	1	1	1
Mn	0.24	0.27	0.19	0.25
Co	0.03	0.07	0.03	0.07
Ni	0.03	0.07	0.03	0.07

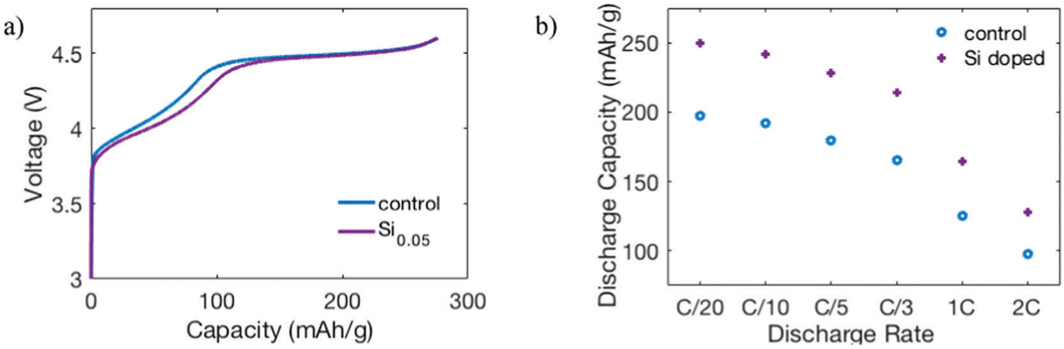

Fig. 1 (a) C/100 first charge voltage profile and (b) rate capability for control and Si-doped HE-NMC.

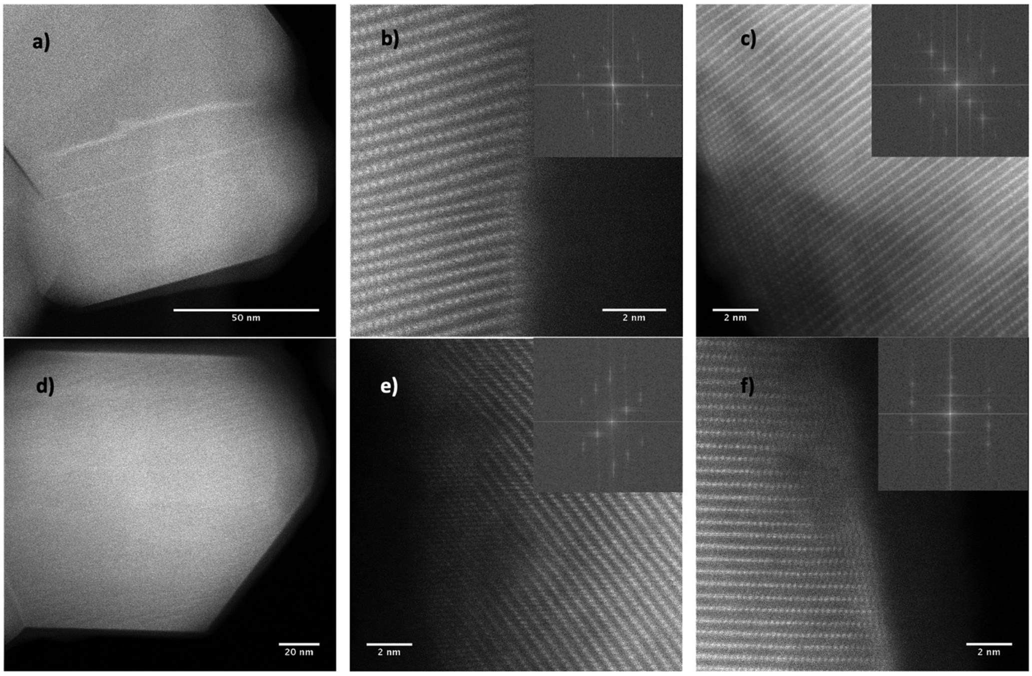

Fig. 2 High resolution STEM images: (a) low magnification pristine control HE-NMC, (b) high magnification pristine control HE-NMC, (c) high magnification pristine $x = 0.05$ Si HE-NMC, (d) low magnification $x = 0.05$ Si HE-NMC cycled to 4.6 V, (e) high magnification control HE-NMC cycled to 4.6 V, and (f) high magnification $x = 0.05$ Si HE-NMC cycled to 4.6 V.

indicating heavier atoms.[21] The bright atomic columns correspond to transition metals layer while the darker columns indicate lithium. For the control material seen in Fig. 2b a thin 1–2 layer boundary layer with little contrast between layers is visible between the layered structure and the amorphous surface. This is evidence of transition metal presence in the lithium layer. After the first charge to 4.6 V, transition metals near the surface migrate to the lithium layer and the boundary layer grows to 5–15 atomic layers in the control material (Fig. 2e) and to approximately 5 layers in the Si-doped material (Fig. 2f). In this study, samples were only imaged at various points during the first cycle. Prior work demonstrates that the thickness and structure of these surface damage layers gradually changes during further cycling. For example, in a simpler Li rich material that did not contain Co or Si, TEM showed a 4 nm thick surface phase after 10 cycles and a 10 nm thick disordered surface phase after 100 cycles.[22]

3.2 Oxidation state change due to Si-doping

Representative EELS for the probed elements (Si, Mn, Co, Ni, and O) in the pristine samples are shown in Fig. 3. The Si-L2,3 edge is observed at 99 eV in the pristine Si sample. The white line ratio of the area of the L_3/L_2 peaks of the transition metal deviates from 2 : 1 by 3d spin–spin coupling and is an indication of the oxidation state.[19] The second derivative method was used to calculate the area under the peaks, where a lower areal ratio indicates an increase in oxidation state. The chemical shifts, determined by the white line ratio method, for Mn, Co, and Ni are −0.01, −0.19, and −0.12 after Si-doping, respectively. The edge onset energy represents the lowest excited

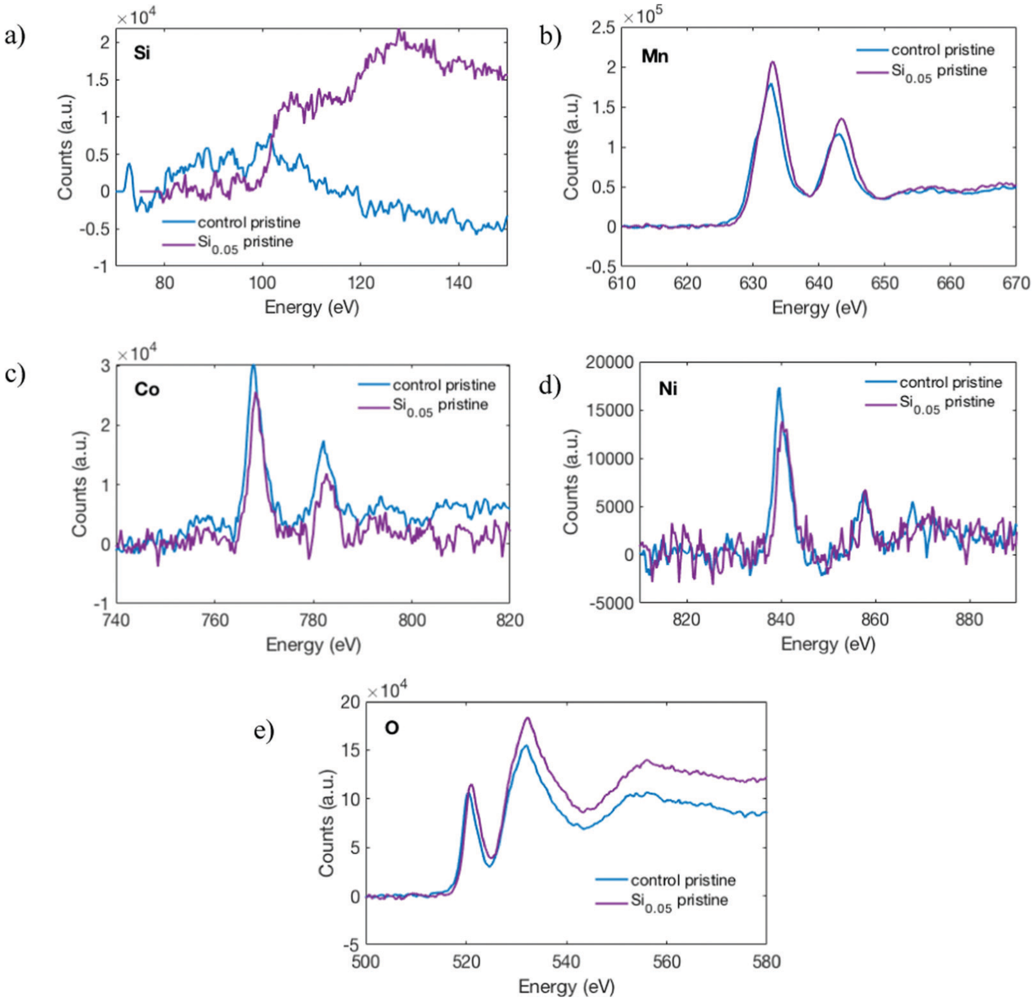

Fig. 3 Pristine control and Si-doped HE-NMC EELS for (a) Si, (b) Mn, (c) Co, (d) Ni and (e) O.

energy level and is defined at the energy corresponding to 10% of the max peak height. A positive shift indicates higher oxidation state. The chemical shifts, determined by the edge onset energy method, for Mn, Co, and Ni are 0.62, 0.78, and 0.89, respectively. Both methods indicate that all of the transition metals are oxidized in the Si-doped material relative to the control (undoped).

In addition to providing information on the electronic states of transition metals, EELS is a preferred technique for probing light elements, including oxygen. In EELS the O K edge provides information on the local oxygen environment. The onset of the O K edge reflects the geometry of the metal–oxygen bonding as well as the oxidation states of the transition metals.[19] The intensity of the O K pre-edge is also related to the transition metal oxidation states.[23] Additionally, the difference in energy between the peak and the pre-peak as well as the intensity ratio of the peaks indicates a change in the oxygen environment.[21] From Fig. 3e the energy difference between the peaks is 0.3 eV higher for the control material, and the intensity ratio of the peak to pre-peak is 10% higher for the doped material.

The EELS analysis shows that all of the peaks shift to higher energies in the pristine Si-doped material (relative to the control). Although the increase of the EELS onset energy for transition metals (TMs) often indicates higher oxidation state, the simultaneous increase in onset energies for oxygen suggests that this shift might be an overall electronic structure change due to Si-doping. At first glance this is somewhat surprising, since the Si composition is only 5% and the Si substitutes with a classical 4^+ charge on the Mn^{4+} lattice site. Assuming uniform dopant distribution, the Si only occupies 5% of the TM sites. At this level, our DFT calculations indicate that the 6 first neighbor O atoms pull closer to the Si, weakening the TM–O bonds on the 6 nearest neighbor TMs around the Si dopant.[17] Furthermore, the DFT results also show that an energetically favorable oxygen vacancy was generated in the neighboring TM layer *via* Si–O–Li–V_O bonding. This long-range interaction impacts 20 second nearest neighbor O atoms and, consequently 30 TM sites for one Si dopant atom. This suggests that all of the transition metals are influenced by 5% Si-doping. Based on this assessment, it is likely that Si-doping lowers the energy level of s and 2p electrons but does not substantially alter the unoccupied 3d electron states, so that increased onset energies occur for both the TMs (L2 and L3) and O (K peak). These energy differences may also lead to changes in bond length due to the stronger Si–O and weaker TM–O bonding in the doped material. This also suggests that Si promotes oxygen vacancy formation from the TM–O bonds that are near the dopants.

3.3 Redox couples during charging

The results in Fig. 1a along with previous work indicate that Si-doped material behaves differently during initial charging.[17,18] The EELS data provides additional insight into this. Fig. 4 shows spectra for each element normalized to the cobalt L_3 peak, as cobalt is expected to have a stable concentration. Results are compared for three conditions: in the as-synthesized pristine state, charged to 4.4 V, and at 4.6 V, the completion of the first charge. The chemical shifts determined by the edge onset method are summarized in Table 2 and those determined by the white line ratio method are presented in

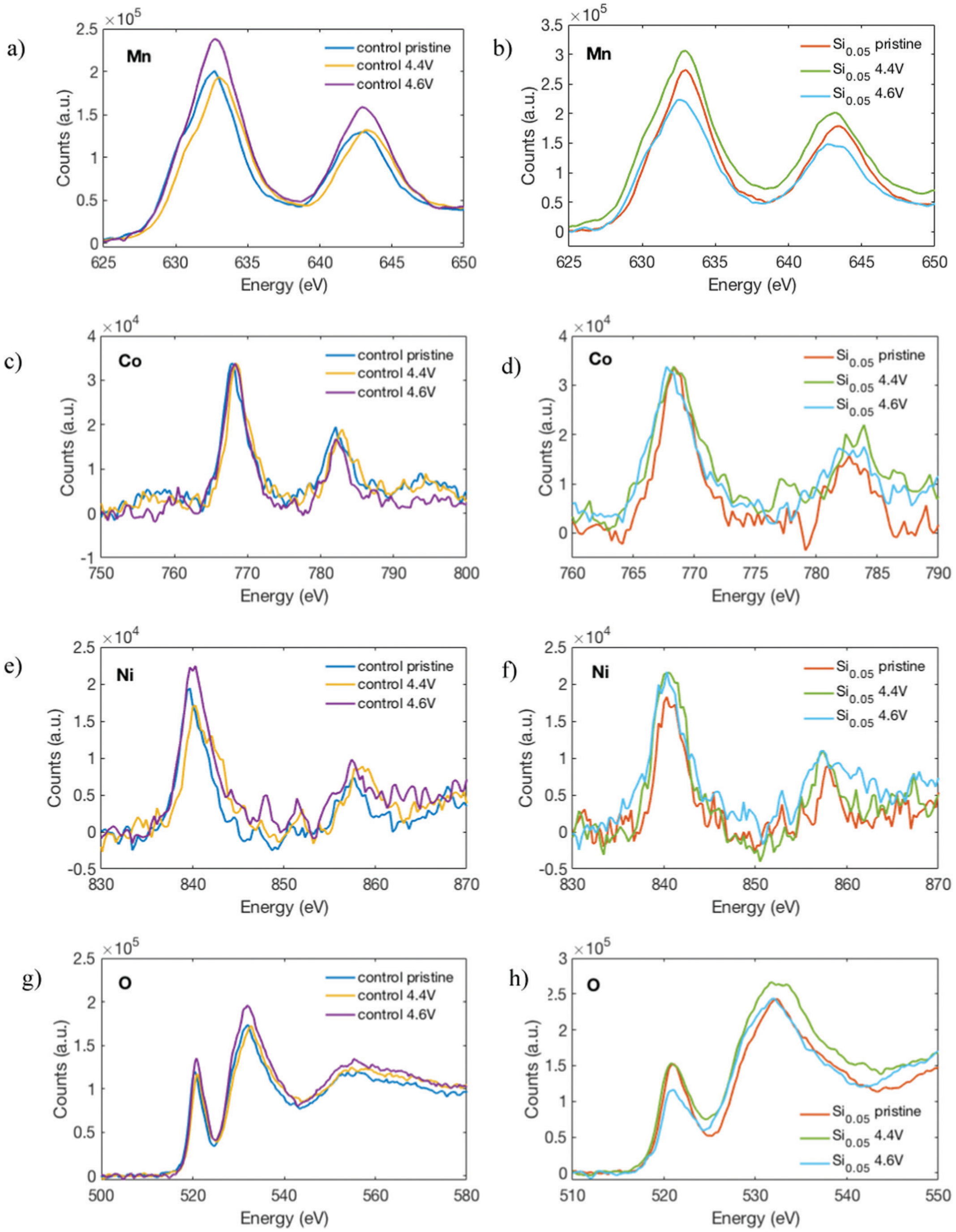

Fig. 4 HE-NMC EELS for (a) control Mn, (b) Si-doped Mn, (c) control Co, (d) Si-doped Co, (e) control Ni, (f) Si-doped Ni, (g) control O, and (h) Si-doped O at various stages throughout the first charge.

Table 2 Chemical shifts determined by the edge onset energy method

	L3 onset energy shift (eV)		
Comparison	Mn	Co	Ni
Relative to pristine control			
4.4 V control	0.43	0.69	0.65
4.6 V control	0.23	−0.13	−0.11
Pristine Si-doped	0.62	0.78	0.89
Relative to pristine Si-doped			
4.4 V Si-doped	−0.81	−1.27	−0.54
4.6 V Si-doped	−0.37	−0.69	−2.44

Table S1 (ESI†). There is good agreement in the two methods used for determining the chemical shift of the transition metal L edge. There is some disagreement in the direction of chemical shift between the two methods for nickel, however, nickel has a relatively low concentration and the data exhibits a lower signal to noise ratio. It is likely that nickel behavior is similar to cobalt, which occurs with the edge onset method. Therefore, the edge onset method (Table 2) is used to describe the chemical shifts for the remainder of this text. EELS results in Table 2 indicate that initial charging of the control HE-NMC material to 4.4 V involves transition metal oxidation; the transition metals are then reduced along the activation plateau. For Si-doped HE-NMC, the transition metals reduce with lithium removal over the sloping portion of the voltage profile and shift to higher oxidation state at the plateau.

The results obtained during charging of the control HE-NMC are all consistent with other reports.[21] The formulated valences of nickel, cobalt, and manganese in the pristine material are approximately 2^+, 3^+, 4^+ and respectively. After charging to 4.4 V, the transition metals shift to higher oxidation state to maintain neutrality after lithium removal (Table 2). The dominant effect here can be described with Kroger–Vink notation, *via*:

$$\mathrm{Li_{Li}^{\times}} + \mathrm{M_M^{\times}} \rightleftarrows \mathrm{V_{Li}'} + \mathrm{M_M^{\bullet}} + \mathrm{Li^{+}} + \mathrm{e'} \qquad (1)$$

For simplicity, this representation assumes that all species are ionic with discrete oxidation states. The Li ions and Li vacancies in the electrode are $\mathrm{Li_{Li}^{\times}}$ and $\mathrm{V_{Li}'}$, and $\mathrm{Li^{+}}$ and $\mathrm{e'}$ refer to the Li ions and electrons that are removed during charging. When a Li ion is removed from the lattice, eqn (1) describes the corresponding change in valence for one of the transition metals, going from initial state, $\mathrm{M_M^{\times}}$, to an oxidized state, $\mathrm{M_M^{\bullet}}$ (*e.g.*, going from +2 to +3, or from +3 to +4, *etc.*). Note that it has been shown that manganese does not oxidize beyond the tetravalent state,[24] so the manganese shift during the charge to 4.4 V suggests that some trivalent manganese is present in the pristine material. This is consistent with the formulation, where charge neutrality corresponds to a small portion of the manganese in the 3^+ state.

DFT results indicate that the process in eqn (1) is more accurately viewed as removing an electron from the hybridized/shared covalent portion of the TM–O bond.[25] This implies that oxygen anions can also participate in redox reactions[26] *via* the following type of process:

$$\mathrm{Li_{Li}^{\times}} + \mathrm{O_O^{\times}} \rightleftarrows \mathrm{V_{Li}'} + \mathrm{O_O^{\bullet}} + \mathrm{Li^{+}} + \mathrm{e'} \qquad (2)$$

With this interpretation, the nature of the TM–O bond is such that Li ion removal is accompanied by oxidation of both the cation and oxygen leading to fractional charge states, rather than the integers indicated in eqn (1) and (2).

With further charging to 4.6 V, the results show that lithium and oxygen removal are accompanied by transition metal reduction, consistent with previous reports.[21,27] In particular, detailed spectroscopy shows that this change occurs primarily near surfaces.[25] This prior work also indicates that the TM oxidation state does not change appreciably in the bulk, which implies that in most of the material Li removal along the plateau is no longer described by eqn (1). Instead, at higher voltages Li loss from the bulk is primarily associated with only anion redox *via* eqn (2) that corresponds to electron removal from an oxygen 2p state that is not associated with TM–O covalent bonding.[25] In contrast, the TM reduction near surfaces (*i.e.*, our experiments for undoped samples) has been associated with the formation of oxygen vacancies,[26] which can lead to charge compensation *via*:

$$\mathrm{Li_{Li}^{\times}} + \mathrm{O_O^{\times}} + \mathrm{M_M^{\bullet}} \rightleftarrows \mathrm{V_{Li}'} + \mathrm{V_O^{\bullet\bullet}} + \mathrm{M_M^{\times}} + \mathrm{Li^{+}} + \mathrm{e'} + \frac{1}{2}\mathrm{O_2}\ (\mathrm{g}) \qquad (3)$$

The oxygen gas evolution shown here has been reported in some experiments,[28] and direct oxidation of the electrolyte is also likely to occur in some situations. In addition to the point defects identified in eqn (1)–(3), the creation of excess lithium and oxygen vacancies facilitates cation migration, with transition metals irreversibly moving into the lithium layer, forming a defect-spinel phase near the surface. This transition metal migration also substantially alters the bulk O redox potential.[25]

At first glance, the results for the Si-doped HE-NMC are counter-intuitive. As the Si-doped material charges to 4.4 V, lithium removal is accompanied by transition metal reduction, requiring another mechanism for charge compensation that is not occurring in the control material. A reasonable explanation for this is that oxygen loss *via* eqn (3) occurs more readily at lower voltages, although other changes in the redox energetics are also potentially relevant. As Si-doped material is charged further to the 4.6 V cutoff, net TM oxidation now accompanies lithium extraction. This suggests that eqn (1) is dominant here (*i.e.*, an electron is removed from the transition metal), which suggests the oxygen loss which leads to net TM reduction is less prevalent in the doped material at these higher voltages. The differences observed during charging to both 4.4 V and 4.6 V are surprising, because they indicate that the non-redox active Si dopant alters the overall redox behavior in the NMC material.

To interpret the behavior observed in the doped material, it is important to recognize that TM oxidation (*via* eqn (1)), anion redox (*via* eqn (2)), and oxygen removal (*via* eqn (3)) can all occur during the charge cycle. However, changes in the energetics of these processes can alter their relative contributions at different voltages. The EELS results reflect net variations due to

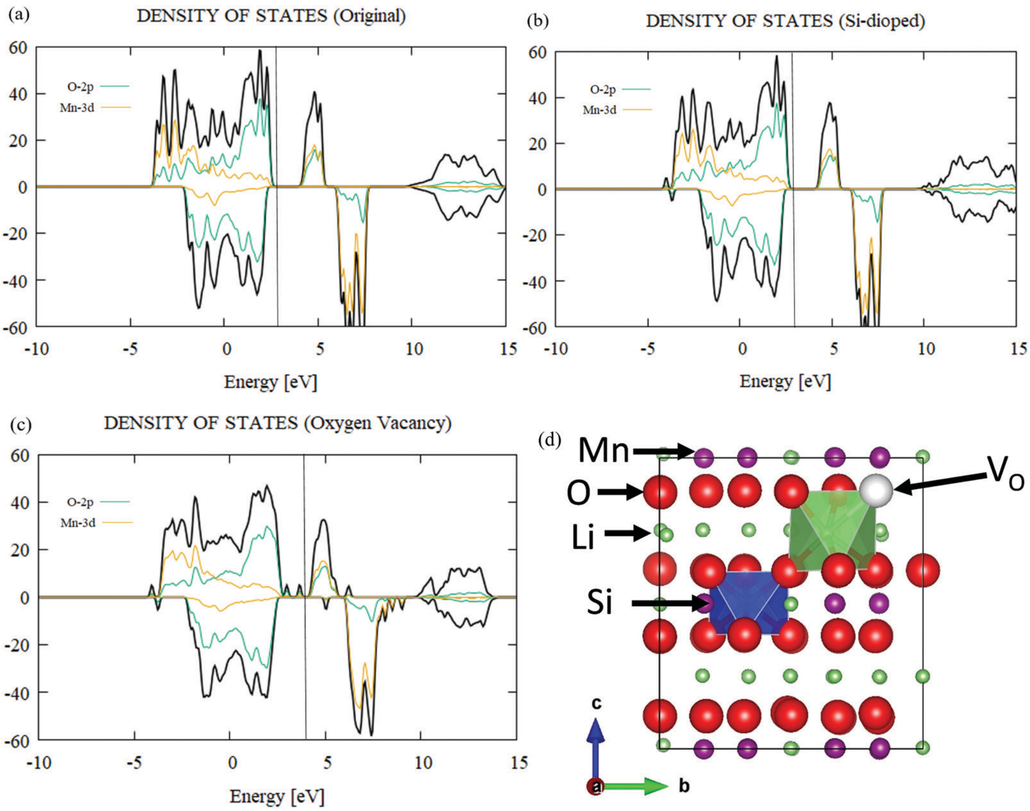

Fig. 5 Partial density of states on Mn-3d orbitals and O-2p orbitals for (a) original Li_2MnO_3, (b) Si-doped Li_2MnO_3 and (c) Si-doped Li_2MnO_3 with one oxygen vacancy. The atomic model for Si-doped Li_2MnO_3 with one oxygen vacancy is shown in (d).

the combined effects of these different mechanisms. In this context, the impact of doping was explored with DFT calculations on the Li_2MnO_3 model system. This provides a reasonable representation of the high-Li content structure that exists in the more complex Li-NMC materials.[5] The results show that Si does not alter the electronic structure of the TM–O bonds, as the partial DOS are very similar for Li_2MnO_3 and Si doped Li_2MnO_3 (see Fig. 5). Other analysis of atomic PDOS and Bader charges also does not show any notable differences between the Si doped and undoped Li_2MnO_3. However, the results show that Si doping can affect oxygen loss. This can be understood from the PDOS plot in Fig. 5c, which indicates that oxygen removal leads to two additional states which belong to both Mn-3d and O-2p near the O vacancies. Electrons in these two additional states require less energy for excitation to the conduction band, in comparison with the electrons in the bulk Li_2MnO_3. Although computing the L_3 and L_2 peaks detected with EELS is not quantitatively accurate with the current DFT+U method, a negative shift of the edge onset energy is qualitatively expected for these electronic states. This shift appears as an oxidation state reduction in EELS and is thus consistent with the experimental observations in the Si-doped samples at 4.4 V. This DFT insight along with the predicted decrease in the oxygen vacancy formation energy supports the idea that Si-doping decreases the oxygen vacancy formation energy and leads to increased oxygen loss along with net transition metal and/or oxygen reduction during initial charging up to 4.4 V, *via* the mechanism in eqn (3). This provides a reasonable explanation for the EELS results before 4.4 V, with oxygen loss compensating for some of the lithium removal, and providing extra charge capacity before the plateau (Fig. 1a). Previous DFT results also show that oxygen vacancies lower the Li vacancy formation energy, thus reducing the voltage required to delithiate.[29] This will lead to increased capacity at the same voltage consistent with the sloping portion of the profile in Fig. 1a, where the capacity at a given voltage is higher in the Si-doped material.

The process outlined above implies that at higher voltages (*i.e.*, along the voltage plateau) there are an increased number of O vacancies in the Si-doped HENMC. With oxygen loss occurring more readily at lower voltages, the amount of oxygen loss that occurs along the plateau may be more limited. Transition metal oxidation due to lithium removal then dominates the compensation mechanism as charging progresses to 4.6 V. During the first charge Si does not change the voltage at the onset of the plateau (Fig. 1a). If Si altered the transition metal redox behavior, this would probably shift the plateau voltage, which suggests that doping does not substantially alter the anion redox and TM restructuring that are believed to occur along the plateau.[25] The largest difference between these two materials is that there is more Li capacity before the plateau is reached. As noted above, this is consistent with the idea that Si enables oxygen loss at lower voltages. This process is not reversible during battery cycling (*i.e.*, O is not reincorporated during discharge), however, the DFT results predict that the additional O vacancies alter the oxygen and transition metal (*i.e.*, Mn in the calculation) redox couples. Thus, while O loss is irreversible, it introduces redox couples that can provide additional reversible capacity (*e.g.*, by converting some Mn^{4+} to Mn^{3+}, *etc.*).

The DFT calculations comparing doped and undoped Li_2MnO_3 show that Si decreases the energy of formation for V_O by 0.05 eV. Additionally, this formation energy does not vary substantially with the distance from the silicon ion.[30] These results suggest that Si-doping will increase the O vacancy concentrations in the pristine materials (prior to cycling). This difference is likely to be relatively small, since all materials are heat treated in air. It is difficult to directly measure these low initial oxygen vacancy concentrations, however, the formation of oxygen vacancies is known to cause volume expansion.[31,32] X-ray diffraction shows that Si-doping leads to a small lattice expansion increase in the pristine material, which is thus consistent with higher O vacancy levels.[17] An increase in oxygen vacancies has also been associated with a decrease in the O K edge pre-peak.[6] Fig. 4g and h show that the relative magnitude of the pre-peak is smaller in all of the Si-doped specimens, which is thus consistent with increased oxygen vacancies. With Si-doping, the intensity of the pre-peak also decreases during the first charge, which supports the idea that oxygen loss is more substantial in these materials. It is also important to note that in the pristine material, the EELS observation showing that Si increases the onset energies for all three transition metals is probably not an indication of TM oxidation state changes. A more likely explanation is that the higher onset energies instead reflect an overall background shift because Si-doping lowers the energy level of s and 2p electrons.

3.4 Non-uniform electronic state distribution within a particle

Changes within the same sample at different depths were also investigated. In the pristine materials, there are minor differences in the transition metal and oxygen spectra from the surface to the bulk. In the doped material Si is observed at all probed locations. The signal is strongest at the surface, but there is clearly Si present inside of the particles as well. This difference may indicate that there is a concentration gradient, but it is also related to an increase in the background signal in the thicker regions of the sample. The overall observations indicate that Si-doping occurs throughout the particle, although the distribution of Si within the particle is unclear. The spatial resolution of the combined EELS-STEM technique shows that the O K edge changes dramatically in the transformed surface layer. The split of the O K edge is an indication of the layered structure;[21] the disappearance of the peak split near the surface suggests a loss of this type of ordering. Oxygen reactions related to electrolyte degradation and the formation of a solid electrolyte interphase layer can affect the interpretation of oxygen bonding effects. However, the spatial resolution of the EELS/STEM technique is capable of showing that the change in the O K edge near the surface directly corresponds to regions of transition metal migration. Fig. 6 shows the EELS for a pixel taken at the surface of a Si-doped HE-NMC particle charged to 4.4 V compared to a pixel in the interior of the particle. This trend was seen in all charged electrodes for both the control and doped material.

With cycling, the oxygen EELS clearly shows spatial variations from the surface to the bulk. This is evident in the comparison

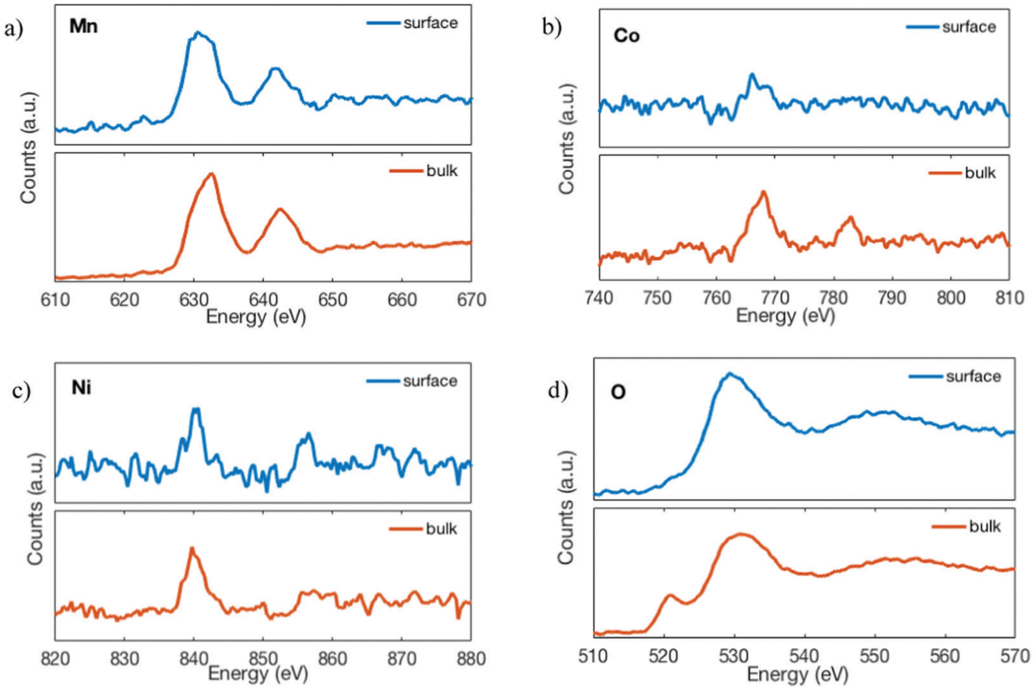

Fig. 6 EELS spectra of Si *x* = 0.05 HE-NMC charged to 4.4 V from a pixel taken at the surface and in the bulk for (a) manganese L-edge, (b) cobalt L-edge, (c) nickel L-edge, and (d) oxygen K-edge.

between surface and bulk spectra for charged Si-doped HE-NMC in Fig. 6. Similar behavior was also observed in the control material (Fig. S1, ESI†). Near the surface of the charged electrodes, the oxygen pre-peak has low intensity. The oxygen pre-peak is related to the transition of the O 1s state to the O 2p state hybridized with TM 3d states.[33] The changes observed here are indicative of a change in the oxygen electronic environment and a deviation from the layered structure, consistent with the splitting of the O K edge that is discussed above. The reduction of the pre-peak on the surface of cycled electrodes has also been attributed to changes in TM 3d states and bonding lengths.[33]

The STEM images in Fig. 2 confirm a layered structure in the Si-doped HE-NMC material. A 5-layer transformed region appears at the surface of the doped sample cycled to 4.6 V. This is approximately half the thickness of the analogous layer in the activated control material. EELS of this surface layer supports the STEM observations of TM migration into the lithium layer. This thinner surface layer is consistent with less transition metal rearrangement in the Si-doped material, and the changes in the oxygen spectra near the surface of the cycled particles are consistent with the idea that the structural differences here are related to oxygen loss. Thus the thinner surface layer in the doped material indicates that Si stabilizes the structure against the phase transformation.

The surface phase transformation is generally related to oxygen loss and transition metal diffusion into the Li-layer. The experimental results indicate that these processes occur in the doped material, but it appears that Si reduces the driving force for the surface transformation by changing the free energy of the initial phase and/or the surface layer. In the doped material the lower oxygen vacancy formation energy is also likely to enhance oxygen diffusion and lead to a more uniform vacancy distribution in the bulk. Our previous experiments with undoped material indicate that significant oxygen vacancy formation occurs well beyond the surface damage layer.[32] A significant vacancy gradient across the particles will be accompanied by more expansion near the surface, since the formation of oxygen vacancies is known to cause lattice expansion.[31,32] Thus, significant oxygen vacancy concentrations will induce net compressive stress. This should increase the driving force for creating the surface layer, since the surface transformation inherently induces tension (*i.e.*, because the new phases are denser than the starting material). A more uniform oxygen vacancy profile across a Si-doped particle will mitigate (or eliminate) the contributions from a compressive stress near the surface. It is not clear if this effect is large enough to fully explain the thinner surface damage layer in the doped materials, but it is a possible contributing factor.

3.5 Nature of the improved electrochemical behavior in the Si-doped material

Si-doping increases the reversible capacity of HE-NMC as well as the rate capability. These observations are consistent with the idea that silicon promotes oxygen loss. Electrochemical data after the first cycle also supports this interpretation (see Fig. 7). For example, the dQ/dV data in Fig. 7b during the second charge shows more capacity in the doped material, with this effect beginning at lower voltages. There is also more capacity in the second discharge of the Si-doped material, which indicates more intrinsic O redox and/or more redox active Mn^{3+}. The shoulder of the 3.7 V peak is shifted to lower voltage relative to the control which is also potentially consistent with increased TM redox activity in the doped material.[25]

The normalized second charge profiles (Fig. 7a) for the doped material are slightly less rate sensitive, which suggests decreased impedance. There are several possible explanations for this. The thinner surface damage layer that forms in the doped material could lead to lower impedance. Also, the variation in transition metal oxidation states in the pristine doped material may facilitate electron conduction. This can also explain the reduced impedance observed in the Si-doped material,[17] and would contribute to a higher capacity at a given cycling rate.

The EELS results show that Si-doping alters oxidation states and redox couples in HE-NMC materials. Multiple factors are likely to contribute to the improved electrochemical performance, but it appears that Si-doping enhances oxygen loss and increases capacity *via* additional redox couples that are associated with oxygen vacancies. This is supported by the DFT findings. Although both anion redox and oxygen vacancy

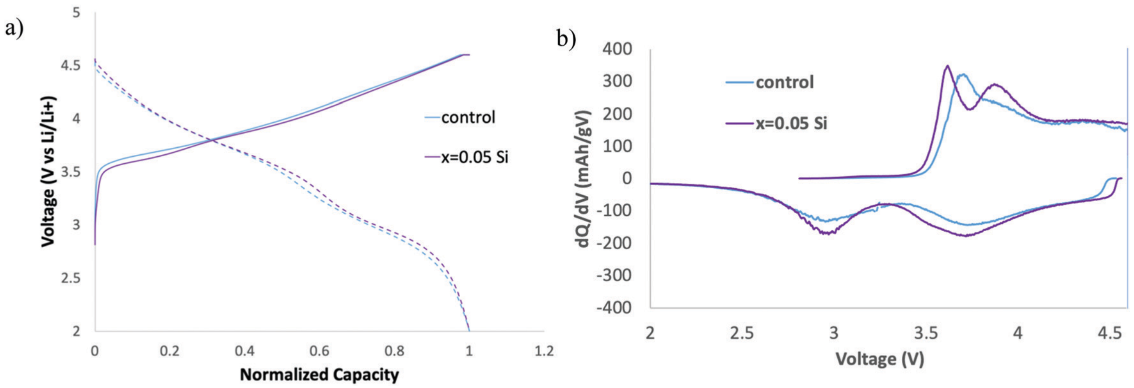

Fig. 7 (a) normalized voltage profile of the second cycle at C/10 c-rate for control and Si-doped HE-NMC and (b) corresponding differential capacity plot.

formation can facilitate cation migration and the surface phase transformation in lithium-rich oxides,[6,34] the anion redox process is reversible whereas oxygen evolution is not. The higher reversible capacity over 40 cycles[17] may in part reflect the smaller amount of active material consumed by structural change at the surface.[6,35,36] However, based on the measured layer thicknesses, this is not the dominant cause. Cation migration that is associated with the surface restructuring is largely irreversible, however, recent work also proposes that reversible cation migration is coupled with anion redox in these materials.[25] While it is possible that Si impacts this complex process, the similar voltage plateau during charging suggests that this is not a major factor. Instead, enhanced oxygen loss is more likely to be the dominant effect. Another possible factor that may reduce the thickness of the surface damage layer is that the increased presence of Ni^{3+} observed in the pristine doped material may reduce Ni and Li mixing, as Ni^{2+} is closer in size to Li^{+}. This will improve cation ordering relative to the control and is consistent with previous Raman results[17] showing structure stability over the first charge as well as less spinel formation observed in the STEM images (Fig. 2) after the 1st charge. As noted above, a reasonable explanation for the increased lattice parameters in the pristine doped material is a higher initial concentration of oxygen vacancies compared to the control.[17] A higher initial concentration of oxygen vacancies could also reduce the formation of additional vacancies during the "activation process" and subsequent cycling.[37] As the activation plateau is partially related to oxygen loss,[1] a shorter plateau (Fig. 1a) may indicate the creation of fewer oxygen vacancies during the "activation process". This along with a higher initial oxygen vacancy concentration in the pristine doped material could contribute to a more uniform distribution of oxygen vacancies, which is consistent with the proposed reduction in near-surface stress in the Si-doped materials that is proposed in Section 3.4.

At first glance, some of our findings seem to disagree with a previous report of Si-doped HE-NMC.[18] Although the stoichiometry is the same, our synthesis method and doping levels are different. Both studies report improved performance with Si-doping, but Ma *et al.* found that Si-doping decreased the lattice volume, and they reported a maximum benefit at $x = 0.02$, whereas our work shows that Si-doping increases the lattice parameters and the benefits increase at higher doping level.[17] Our previous DFT results agree with this prior work and show strong Si–O bonding, such that this oxygen is difficult to remove. However, oxygen vacancies that are not adjacent to the silicon have a lower oxygen vacancy formation energy. This analysis has now been extended to account for changes in the redox behavior of the Si-doped samples.

IV. Conclusions

Si-doping increases the capacity of $Li_{1.2}Mn_{0.54}Ni_{0.13}Co_{0.13}O_2$ (HE-NMC) and stabilizes its structure during cycling. The near surface structure of control and Si-doped HE-NMC was investigated with STEM. This shows that after the first charge cycle, the surface phase transformation in the doped material is less extensive. The electronic states during the first electrochemical charge cycle were studied with EELS. From this, it is clear that doping produces changes that are more complex than simple inactive Si^{4+}/Mn^{4+} substitution where the dopant only pins the structure. The changes observed demonstrate that Si modulates the redox behavior of HE-NMC. DFT predictions reveal that this Si-doping alters the redox sequence by favoring oxygen vacancy formation in the pristine material. This leads to extra electronic states near the Fermi level on the TMs such that they are reduced during the first charge cycle. The complex nature of the Si-doping effects on first charge redox chemistry requires further study. However, the findings reported here demonstrate that it is possible to substantially improve electrochemical performance by employing a non-redox active dopant that alters the redox processes that are associated with the other components in the material.

Conflicts of interest

There are no conflicts to declare.

Acknowledgements

This work is supported by the National Science Foundation under Grants No. DMR-1410850 and 1832829. All the calculations were performed on the HPCC at MSU. We also acknowledge Thomas Blum and Wen Sun at ORNL for their assistance with transmission electron microscope characterization. Christine James provided assistance with the setup for the DFT calculations. The microscopy work were completed at the Center for Nanophase Materials Sciences, which is a DOE Office of Science User Facility. XL and MC was sponsored by the U.S. DOE Basic Energy Sciences, Materials Sciences and Engineering Division.

References

1 A. R. Armstrong, M. Holzapfel, P. Novák, C. S. Johnson, S.-H. Kang, M. M. Thackeray and P. G. Bruce, Demonstrating oxygen loss and associated structural reorganization in the lithium battery cathode Li[Ni0.2Li0.2Mn 0.6]O2, *J. Am. Chem. Soc.*, 2006, **128**, 8694–8698.

2 P. E. Pearce, A. J. Perez, G. Rousse, M. Saubanère, D. Batuk, D. Foix, E. McCalla, A. M. Abakumov, G. Van Tendeloo, M.-L. Doublet and J.-M. Tarascon, Evidence for anionic redox activity in a tridimensional-ordered Li-rich positive electrode β-Li_2IrO_3, *Nat. Mater.*, 2017, **16**, 580–586.

3 J. Xu, M. Sun, R. Qiao, S. E. Renfrew, L. Ma, T. Wu, S. Hwang, D. Nordlund, D. Su, K. Amine, J. Lu, B. D. McCloskey, W. Yang and W. Tong, Elucidating anionic oxygen activity in lithium-rich layered oxides, *Nat. Commun.*, 2018, **9**, 947.

4 B. Qiu, M. Zhang, Y. Xia, Z. Liu and Y. S. Meng, Understanding and Controlling Anionic Electrochemical Activity in High-Capacity Oxides for Next Generation Li-Ion Batteries, *Chem. Mater.*, 2017, **29**(3), 908–915.

5 D.-H. Seo, J. Lee, A. Urban, R. Malik, S. Kang and G. Ceder, The structural and chemical origin of the oxygen redox activity in layered and cation-disordered Li-excess cathode materials, *Nat. Chem.*, 2016, **8**, 692–697.

6 D. Qian, B. Xu, M. Chi and Y. S. Meng, Uncovering the roles of oxygen vacancies in cation migration in lithium excess layered oxides, *Phys. Chem. Chem. Phys.*, 2014, **16**, 14665–14668.

7 D. Mohanty, J. Li, D. P. Abraham, A. Huq, E. A. Payzant, D. L. Wood and C. Daniel, Unraveling the voltage-fade mechanism in high-energy-density lithium-ion batteries: Origin of the tetrahedral cations for spinel conversion, *Chem. Mater.*, 2014, **26**(21), 6272–6280.

8 M. Bettge, Y. Li, K. G. Gallagher, Y. Zhu, Q. Wu, W. Lu, I. Bloom and D. P. Abraham, Voltage Fade of Layered Oxides: Its Measurement and Impact on Energy Density, *J. Electrochem. Soc.*, 2013, **160**, A2046–A2055.

9 Y. Wu, C. Ma, J. Yang, Z. Li, L. F. Allard, C. Liang and M. Chi, Probing the Initiation of Voltage Decay in Li-Rich Layered Cathode Materials at Atomic Scale, *J. Mater. Chem. A*, 2015, **3**, 5385–5391.

10 P. K. Nayak, J. Grinblat, M. Levi, E. Levi, S. Kim, J. W. Choi and D. Aurbach, Al Doping for Mitigating the Capacity Fading and Voltage Decay of Layered Li and Mn-Rich Cathodes for Li-Ion Batteries, *Adv. Energy Mater.*, 2016, **6**(8), 1502398.

11 R. Yu, G. Wang, M. Liu, X. Zhang, X. Wang, H. Shu, X. Yang and W. Huang, Mitigating voltage and capacity fading of lithium-rich layered cathodes by lanthanum doping, *J. Power Sources*, 2016, **335**, 65–75.

12 Y. Zhao, M. Xia, X. Hu, Z. Zhao, Y. Wang and Z. Lv, Effects of Sn doping on the structural and electrochemical properties of $Li_{1.2}Ni_{0.2}Mn_{0.8}O_2$ Li-rich cathode materials, *Electrochim. Acta*, 2015, **174**, 1167–1174.

13 J. H. Song, A. Kapylou, H. S. Choi, B. Y. Yu, E. Matulevich and S. H. Kang, Suppression of irreversible capacity loss in Li-rich layered oxide by fluorine doping, *J. Power Sources*, 2016, **313**, 65–72.

14 B. Seteni, N. Rapulenyane, J. C. Ngila, S. Mpelane and H. Luo, Coating effect of $LiFePO_4$ and Al_2O_3 on $Li_{1.2}Mn_{0.54}Ni_{0.13}Co_{0.13}O_2$ cathode surface for lithium ion batteries, *J. Power Sources*, 2017, **353**, 210–220.

15 Z. Wang, E. Liu, L. Guo, C. Shi, C. He, J. Li and N. Zhao, Cycle performance improvement of Li-rich layered cathode material $Li[Li_{0.2}Mn_{0.54}Ni_{0.13}Co_{0.13}]O_2$ by ZrO_2 coating, *Surf. Coat. Technol.*, 2013, **235**, 570–576.

16 B. Li and D. Xia, Anionic Redox in Rechargeable Lithium Batteries, *Adv. Mater.*, 2017, **29**, 1701054.

17 L. Nation, Y. Wu, C. James, Y. Qi, B. R. Powell and B. W. Sheldon, Si-doped high-energy $Li_{1.2}Mn_{0.54}Ni_{0.13}Co_{0.13}O_2$ cathode with improved capacity for lithium-ion batteries, *J. Mater. Res.*, 2018, **33**, 4182–4191.

18 J. Ma, H. Yan, B. Li, Z. Xia, W. Huang, L. An and D. Xia, Tuning the Electronic Structure of the Metal–Oxygen Group by Silicon Substitution in Lithium-Rich Manganese-Based Oxides for Superior Performance, *J. Phys. Chem. C*, 2016, **120**, 13421–13426.

19 H. Tan, J. Verbeeck, A. M. Abakumov and G. Van Tendeloo, Oxidation state and chemical shift investigation in transition metal oxides by EELS, *Ultramicroscopy*, 2012, **116**, 24–33.

20 Y. Shin, H. Ding and K. A. Persson, Revealing the Intrinsic Li Mobility in the Li 2 MnO 3 Lithium-Excess Material, *Chem. Mater.*, 2016, **28**, 2081–2088.

21 C. R. Fell, D. Qian, K. J. Carroll, M. Chi, J. L. Jones and Y. S. Meng, Correlation Between Oxygen Vacancy, Microstrain, and Cation Distribution in Lithium-Excess Layered Oxides During the First Electrochemical Cycle, *Chem. Mater.*, 2013, **25**, 1621–1629.

22 J. Zheng, P. Xu, M. Gu, J. Xiao, N. D. Browning, P. Yan, C. Wang and J.-G. Zhang, Structural and Chemical Evolution of Li- and Mn-Rich Layered Cathode Material, *Chem. Mater.*, 2015, **27**, 1381–1390.

23 F. Lin, I. M. Markus, M. M. Doeff and H. L. Xin, Chemical and structural stability of lithium-ion battery electrode materials under electron beam, *Sci. Rep.*, 2014, **4**, 5694.

24 K. Kubobuchi, M. Mogi, H. Ikeno, I. Tanaka, H. Imai and T. Mizoguchi, Mn $L_{2,3}$-edge X-ray absorption spectroscopic studies on charge-discharge mechanism of Li_2 MnO_3, *Appl. Phys. Lett.*, 2014, **104**, 053906.

25 W. E. Gent, K. Lim, Y. Liang, Q. Li, T. Barnes, S. J. Ahn, K. H. Stone, M. McIntire, J. Hong, J. H. Song, Y. Li, A. Mehta, S. Ermon, T. Tyliszczak, D. Kilcoyne, D. Vine, J. H. Park, S. K. Doo, M. F. Toney, W. Yang, D. Prendergast and W. C. Chueh, Coupling between oxygen redox and cation migration explains unusual electrochemistry in lithium-rich layered oxides, *Nat. Commun.*, 2017, **8**, 2091.

26 H. Koga, L. Croguennec, M. Ménétrier, P. Mannessiez, F. Weill and C. Delmas, Different oxygen redox participation for bulk and surface: A possible global explanation for the cycling mechanism of $Li_{1.20}Mn_{0.54}Co_{0.13}Ni_{0.13}O_2$, *J. Power Sources*, 2013, **236**, 250–258.

27 E. Hu, X. Yu, R. Lin, X. Bi, J. Lu, S. Bak, K. W. Nam, H. L. Xin, C. Jaye, D. A. Fischer, K. Amine and X. Q. Yang, *Nat. Energy*, 2018, 690–698.

28 R. Jung, M. Metzger, F. Maglia, C. Stinner and H. A. Gasteiger, Oxygen Release and Its Effect on the Cycling Stability of $LiNi_xMn_yCo_zO_2$ (NMC) Cathode Materials for Li-Ion Batteries, *J. Electrochem. Soc.*, 2017, **164**, A1361–A1377.

29 C. James, Y. Wu, B. W. Sheldon and Y. Qi, The impact of oxygen vacancies on lithium vacancy formation and diffusion in $Li_{2-x}MnO_{3-\delta}$, *Solid State Ionics*, 2016, **289**, 87–94.

30 C. James, PhD thesis, MSU, 2019.

31 C. James, Y. Wu, B. W. Sheldon and Y. Qi, Computational Analysis of Coupled Anisotropic Chemical Expansion in $Li_{2-x}MnO_{3-\delta}$, *MRS Adv.*, 2016, **1**, 1037–1042.

32 L. Nation, J. Li, C. James, Y. Qi, N. Dudney and B. W. Sheldon, *In situ* stress measurements during electrochemical cycling of lithium-rich cathodes, *J. Power Sources*, 2017, **364**, 383–391.

33 B. Xu, C. R. Fell, M. Chi and Y. S. Meng, Identifying surface structural changes in layered Li-excess nickel manganese oxides in high voltage lithium ion batteries: A joint experimental and theoretical study, *Energy Environ. Sci.*, 2011, **4**, 2223.

34 J.-M. Lim, D. Kim, Y.-G. Lim, M.-S. Park, Y.-J. Kim, M. Cho and K. Cho, The origins and mechanism of phase transformation in bulk Li_2MnO_3: first-principles calculations and experimental studies, *J. Mater. Chem. A*, 2015, **3**, 7066–7076.

35 M. M. Thackeray, S.-H. Kang, C. S. Johnson, J. T. Vaughey, R. Benedek and S. A. Hackney, Li_2MnO_3-stabilized $LiMO_2$ (M = Mn, Ni, Co) electrodes for lithium-ion batteries, *J. Mater. Chem.*, 2007, **17**, 3112.

36 D. Mohanty, S. Kalnaus, R. A. Meisner, K. J. Rhodes, J. Li, E. A. Payzant, D. L. Wood and C. Daniel, Structural transformation of a lithium-rich $Li_{1.2}Co_{0.1}Mn_{0.55}Ni_{0.15}O_2$ cathode during high voltage cycling resolved by *in situ* X-ray diffraction, *J. Power Sources*, 2013, **229**, 239–248.

37 B. Qiu, M. Zhang, L. Wu, J. Wang, Y. Xia, D. Qian, H. Liu, S. Hy, Y. Chen, K. An, Y. Zhu, Z. Liu and Y. S. Meng, Gas–solid interfacial modification of oxygen activity in layered oxide cathodes for lithium-ion batteries, *Nat. Commun.*, 2016, **7**, 12108.